Quantum Coherence Times Enhancement in Vanadium(IV)-based Potential Molecular Qubits: The Key Role of the Vanadyl Moiety

(Article begins on next page)

02 July 2024

This is the author's final version of the contribution published as:

The publisher's version is available at:

When citing, please refer to the published version.

Link to this full text:
http://hdl.handle.net/

iris - AperTO

Quantum Coherence Times Enhancement in Vanadium(IV)-based Potential Molecular Qubits: the Key Role of the Vanadyl Moiety

Matteo Atzori,*,† Elena Morra,‡ Lorenzo Tesi,† Andrea Albino,† Mario Chiesa,‡ Lorenzo Sorace,† and Roberta Sessoli*,†

† Dipartimento di Chimica "Ugo Schiff" e INSTM, Università degli Studi di Firenze, Via della Lastruccia 3, I50019 Sesto Fiorentino (Firenze), Italy

‡ Dipartimento di Chimica e NIS Centre, Università di Torino, Via P. Giuria 7, I10125 Torino, Italy

ABSTRACT: In the search for long-lived quantum coherence in spin systems, vanadium(IV) complexes have shown record phase memory times among molecular systems. When nuclear spin-free ligands are employed, vanadium(IV) complexes can show at low temperature sufficiently long quantum coherence times, T_m, to perform quantum operations, but their use in real devices operating at room temperature is still hampered by the rapid decrease of T_1 caused by the efficient spin-phonon coupling. In this work we have investigated the effect of the different coordination environment on the magnetization dynamics and the quantum coherence of two vanadium(IV)-based potential molecular spin qubits in the solid state by introducing a unique structural difference, *i.e.* an oxovanadium(IV) in a square pyramidal *versus* a vanadium(IV) in an octahedral environment featuring the same coordinating ligand, namely the 1,3-dithiole-2-thione-4,5-dithiolate. This investigation, performed by a combined approach of alternate current (AC) susceptibility measurements, and continuous wave (CW) and pulsed electron paramagnetic resonance (EPR) spectroscopies revealed that the effectiveness of the vanadyl moiety in enhancing quantum coherence up to room temperature is related to a less effective mechanism of spin-lattice relaxation that can be quantitatively evaluated by the exponent n (ca. 3) of the temperature dependence of the relaxation rate. A more rapid collapse is observed for the non-oxo counterpart ($n = 4$) hampering the observation of quantum coherence at room temperature. Record coherence time at room temperature (1.04 μs) and Rabi oscillations are also observed for the vanadyl derivative in a very high concentrated material (5±1%) as a result of the additional benefit provided by the use of a nuclear spin-free ligand.

INTRODUCTION

Quantum computation, one of the pillars of the technological revolution that is foreseen for the next decades, has its core in the quantum bit, or qubit,[1,2] *i.e.* a two states quantum-mechanical system able to be placed in a state of coherent superposition of these two states.[3] Physical realizations of qubits can be found in superconductive circuits, trapped ions, and can be based on photons, spins, *etc.*[3,4] Among them, spins, both nuclear and electronic, are particularly interesting because the superposition of spin states can be realized by accessible pulsed magnetic resonance techniques. The most investigated electronic spin systems are nitrogen-vacancy pairs in diamond[5,6] or defects in silicon[7] or silicon carbide.[8] In this context, magnetic molecules can play a key role due to the wide range of physical properties they exhibit and the intrinsic quantum nature of some of them. Both "static" and "dynamic" components of a quantum computer can be in principle realized by exploiting, for the former, the magnetic bistability due to the magnetic anisotropy and the large spin of single-molecule magnets (SMMs),[9] and for quantum logic operations the long coherence that characterizes molecules with an isotropic small spin. Recently, the interest has been extended to forbidden spin transitions in molecules with $S > 1/2$,[10] as well as to lanthanide complexes in highly symmetric coordination environments.[11,12] The realization of a qubit requires, however, the accomplishment of stringent and somehow conflicting prerequisites known as Di Vincenzo criteria,[13] and their preparation and investigation represent a current and very challenging research field. Molecule-based systems like polynuclear metal complexes[1,2,14] are currently investigated for the possibility offered by synthetic chemistry to obtain multi-bit systems with controlled exchange interaction between them.[15] Despite the advantage of chemical tunability of molecular systems with respect to classical inorganic materials, the short lifetime of the quantum superposition of states, represented by the spin-spin relaxation time T_2 or the phase memory time T_m, has up to now posed important limitations in their perspective use as qubits. Even if coherence can be significantly enhanced by exploiting atomic clock transitions between hyperfine states, as recently reported for a Ho(III) polyoxometallate,[12] the most promising systems remain $S = 1/2$ complexes.[16,17] Remarkably, mononuclear V^{IV} complexes with nuclear spin-free ligands like dithiolenes,[18] when dispersed in a nuclear spin-free solvent, CS_2, can attain, at low temperature, T_m of the order of the millisecond,[19] a value comparable to those observed for vacancies in extended lattices. Their use at room temperature is however hampered by the rapid decrease, on increasing the temperature, of the spin-lattice relaxation time, T_1,

which acts as a limiting factor for T_m, as well as by the loss of a rigid structure provided by the frozen solution.

In a recent investigation we have shown that alternate current (AC) susceptometry can flank pulsed electron paramagnetic resonance (EPR) techniques to identify species that show slow spin-lattice relaxation.[20] A vanadyl complex with a β-diketonate ligand has revealed remarkable T_m despite the proton rich ligands, and, more interestingly, a long T_1 over a wide range of temperature and applied magnetic fields.[20] We have then extended these studies to a multifunctional and processable potential molecular spin system, the vanadyl phthalocyanine, by preparing crystalline materials with different percentage of paramagnetic component diluted in the diamagnetic host titanyl phthalocyanine.[21] This allowed to extend the investigation of the quantum coherence up to room temperature leading to a remarkable T_m of ca. 1 μs at 300 K, representing the highest value obtained to date for molecular electronic spin qubits.[21] Rabi oscillations were also observed in this nuclear spin-active environment (^{1}H and ^{14}N nuclei) at room temperature, indicating an outstanding robustness of the quantum coherence in these vanadyl-based systems.

Both the robustness of the quantum coherence of V^{IV} in a oxovanadium(IV) environment[20,21] and the benefit provided by employing nuclear spin-free ligand,[18,19] are then tangible clues for coherence time optimization. We have combined these features to prepare a novel optimized molecular system as a potential spin qubit, and prove the effectiveness of the vanadyl moiety in the enhancement of the quantum coherence times by comparing its properties with those of a non-oxo V^{IV} complex with the same ligand. We have thus investigated the magnetic relaxation and the quantum coherence in solid crystalline phase of two potential molecular spin qubits, [(Ph)$_4$P]$_2$[VO(dmit)$_2$] (**1**) and [(Ph)$_4$P]$_2$[V(dmit)$_3$] (**2**) (dmit = 1,3-dithiole-2-thione-4,5-dithiolate), by means of a multitechnique approach based on AC susceptibility measurements, and pulsed electron paramagnetic resonance spectroscopy. Experiments performed on 5±1% crystalline dispersions of **1** and **2** in their isostructural diamagnetic hosts [(Ph)$_4$P]$_2$[MoO(dmit)$_2$] (**3**) and [(Ph)$_4$P]$_2$[Ti(dmit)$_3$] (**4**), respectively, namely [(Ph)$_4$P]$_2$[VO$_{0.05}$MoO$_{0.95}$(dmit)$_2$] (**5**) and [(Ph)$_4$P]$_2$[V$_{0.06}$Ti$_{0.94}$(dmit)$_3$] (**6**), allowed to investigate the magnitude and the temperature dependence of the relaxation times. In order to evaluate the contribution to the decoherence provided by ^{1}H nuclei, we have also prepared a 5±1% VO/MoO crystalline dispersion, an analogue to compound **5**, where the (Ph)$_4$P$^+$ counterion have been replaced with the deuterated cation d_{20}-(Ph)$_4$P$^+$, [(d_{20}-Ph)$_4$P]$_2$[VO$_{0.05}$MoO$_{0.95}$(dmit)$_2$] (**5'**). The difference in the observed relaxation times for **1** and **2**, and their crystalline dispersions **5** and

6, are discussed on the basis of the unique structural difference introduced in the two selected systems, *i.e.* oxovanadium(IV) *versus* vanadium(IV) moieties, and the resultant coordination geometry change, *i.e.* square pyramidal *versus* octahedral, representing a fundamental step in the identification of key design criteria for the enhancement of the quantum coherence time in molecule-based systems.

RESULTS AND DISCUSSION

Synthesis of Pure Compounds and Doped Materials Preparation. Compounds **1** and **3** were obtained through a common synthetic strategy by slightly changing what already reported in the literature for the preparation of **3**.[22] The reaction between the dmit^{2-} ligand, obtained *in situ* by deprotecting 4,5-bis(benzoylthio)-1,3-dithiole-2-thione with sodium methoxide, and vanadyl(IV) sulfate or pyridinium molybdenyl(V)pentachloride, allowed to obtain compounds **1** and **3**, respectively, in good yields (Scheme 1a).
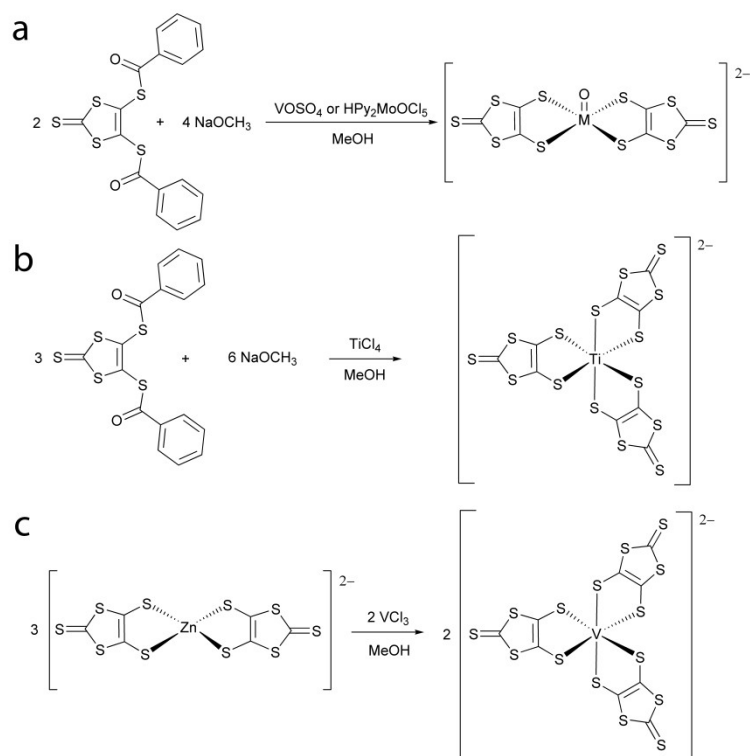
Scheme 1. Reaction schemes for the synthesis of **1** and **3** (a), **2** (c), and **4** (b).

While compound **4** was obtained through a similar procedure with respect to that adopted for **1** and **3** by reacting the deprotected dmit^{2-} ligand with TiCl$_4$ (Scheme 1b), compound **2** was more conveniently obtained by a metal ion substitution operated by reacting VCl$_3$ with [(Ph)$_4$P]$_2$[Zn(dmit)$_2$], in accordance with what already reported in the past (Scheme 1c).[23] It

should be mentioned that an alternative synthesis based on the reaction of VCl_3 with the uncoordinated $dmit^{2-}$ ligand under inert atmosphere, similarly to what more recently reported,[19] resulted in the formation of a mixture of the desired product **2** and the diamagnetic monoanionic oxidized species $[(Ph)_4P][V(dmit)_3]$ (**7**) that has been structurally characterized (see Supporting Information).

The preparation of the crystalline dispersions **5**, **5'** and **6** were performed following two different approaches as a consequence of the different solubility features exhibited by the bis-chelated and tris-chelated derivatives. To overcome the reduced solubility of **1** and **3**, the crystalline dispersions **5** and **5'** were obtained through a direct synthesis between weighted amounts of VO^{2+} (5% molar) and MoO^{2+} (95% molar) metal ions sources (*vide supra*) and the $dmit^{2-}$ ligand, as done for the preparation of the pure compounds. **6** was otherwise obtained by dissolution of weighted amounts of the pure compounds **2** (5% molar) and **4** (95% molar) in acetone and subsequent precipitation by solvent evaporation under reduced pressure.

While the choice of using a Ti^{IV} complex as diamagnetic host for a V^{IV} paramagnetic system appears quite expectable, the choice of using a molybdenyl(IV)-based system as diamagnetic host for a vanadyl one deserves some comments. This choice was dictated by the lack of stable titanyl-based heteroleptic coordination compounds, especially with coligands having oxygen or sulphur as donor atoms. An elegant way to overcome this drawback is to exploit the ability of dithiolene ligands, such as $dmit^{2-}$ ligand selected for this study, to promote the stabilization of a square pyramidal coordination geometry of the Mo^{IV} ion featuring a single Mo=O double bond.[22] This provides the same coordination environment usually exhibited by vanadyl-based mononuclear compounds, thus allowing to realize crystalline dispersions of a vanadyl complex in an isostructural matrix based on an apparently dissimilar metal ion.

Crystal Structures. Although the preparation of a coordination compound containing the dianionic complex $[VO(dmit)_2]^{2-}$ was already claimed in the past,[23] no structural data were reported so far. Single crystals suitable for X-ray diffraction analysis of compounds **1** and **3** were obtained by slow evaporation of acetone solutions. Compounds **1** and **3** are isostructural and crystallize in the monoclinic *C2/c* space group with half of the anionic complex and one tetraphenylphosphonium counterion in the asymmetric unit. Their crystal structure consists of $[MO(dmit)_2]^{2-}$ (M = V^{IV}, Mo^{IV}) anions alternate in M=O up and M=O down configurations separated by tetraphenylphosphonium cations (Figure S1). The shortest M⋯M distances are in the 10.50–15.79 Å and 10.69–15.51 Å ranges, for **1** and **3**, respectively. Very few

intramolecular contacts shorter than the sum of the van der Waals radii are observed between metal complexes, most of them involving the cations.

The molecular structures of the dianionic complex of **1** and **3** are shown in Figure 1. Both systems present a distorted square pyramidal coordination geometry with the metal ions slightly above the basal plane (0.68 Å (**1**) and 0.72 Å (**3**)). The apical position is occupied by an oxo ligand which forms a double bond with the M^{IV} ions with a M=O bond distance of 1.594 Å and 1.689 Å, for **1** and **3**, respectively, whereas the M−S single bond lengths are 2.386 and 2.387 Å for **1** and 2.394 and 2.402 Å for **3**.
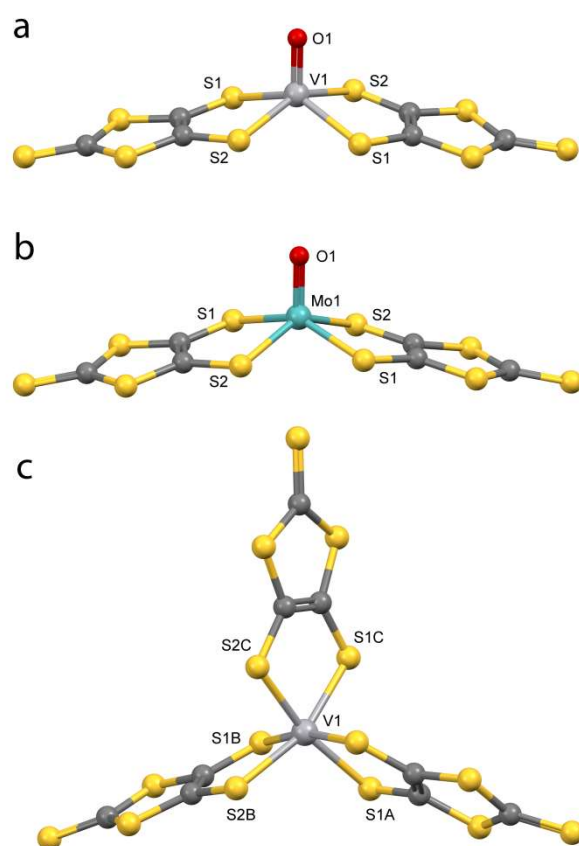
Figure 1. Molecular structure of the dianionic complexes of compounds **1** (a), **2** (c), and **3** (b) with principal atoms labelling scheme.

The presence of a short M=O bond is responsible for a d-orbitals splitting of the metal centres that leaves the d_{xy} orbital lowest in energy and well separated from the other orbitals. This, together with a single unpaired electron of the $S = 1/2$ V^{IV} ion, makes **1** a perfect two levels state potential molecular qubit. On the contrary, the two d-electrons of the Mo^{IV} occupy the same d-orbital and are paired in a low spin configuration, making **3** a useful diamagnetic matrix (*vide supra*).

Single crystals suitable for X-ray diffraction analysis of compound **2** were obtained by slow diffusion of diethyl ether in an acetone solution. Compound **2** crystallizes in the monoclinic *P2$_1$/c* with one anionic complex and two tetraphenylphosphonium counterions in the asymmetric unit. The crystal structure consists of homoleptic tris-chelated [V(dmit)$_3$]$^{2-}$ anions showing Λ and Δ chirality and tetraphenylphosphonium cations (Figure S2). The shortest M···M distances are in the 9.75–15.98 Å range and are comparable to those observed for **1** and **3**. Also in this case, few S···S contacts shorter than the sum of the van der Waals radii between metal complexes are observed, whereas the interactions with the counterions dominate.

The molecular structure of the complex anion of **2** is reported in Figure 1. The coordination geometry around the V^{IV} ion is a distorted octahedron with an average V–S distance of 2.386 Å, an average twist angle of 41.0°, and an average chelate fold angle of 7.2°.[24] All these structural parameters are in good agreement with those observed in the already reported crystal structures of compounds containing this complex anion with a different counterion[23] and with that of a recently reported structure of an acetone solvate of **2**.[19] These structural parameters match well with those reported for similar dianionic tris-chelated V^{IV} complexes with dithiolenes ligands, and confirm their effectiveness to evaluate the oxidation states of both the metal centers and the dithiolenes ligands in these redox-active systems.[24] In this case, the ligand field symmetry is responsible for a *d* orbital splitting that leaves the d_z^2 orbital (where *z* is the trigonal axis of the distorted octahedron) lowest in energy with respect to the other orbitals, as evidenced by EPR spectroscopy (*vide infra*) and by density functional theory calculations (DFT) on analogous vanadium(IV)-based tris-chelated complexes.[24]

In all structurally characterized compounds (**1-3**) the intraligand bond distances are in the usual range for the coordinated dianionic unoxidized dmit^{2-} ligand (Table S1). All attempts to crystallize **4** were unsuccessful; however, powder X-ray diffraction (PXRD) measurements performed on a polycrystalline sample of **4** clearly show that this compound is isostructural with its V^{IV} analogue **2** (Figure S3).

PXRD analyses were performed on polycrystalline samples of all investigated systems, both pure compounds (**1-4**) and crystalline dispersions (**5, 5'** and **6**), to ascertain their structural phase homogeneity. This is clearly evidenced by the good agreement between experimental and simulated patterns (Figures S4-S7).

Magnetization dynamics. Compounds **1** and **2** have been investigated by AC susceptometry in order to get deeper insights on their magnetization dynamics. The thermal variation of the magnetic susceptibility in a zero static magnetic field reveals no imaginary component of the

susceptibility (χ'') in the whole investigated temperature range (2.0–40 K for **1**, and 2.0–10 K for **2**). When a small static magnetic field (> 40 mT) is applied, slow magnetic relaxation is observed with appearance of a peak in the imaginary component of the susceptibility and a concomitant decrease of the real part (χ') (Figures S8-S14). Both compounds **1** and **2** under a static magnetic field of 0.2 T show slow relaxation of the entire magnetization, so that, this field was selected to investigate the temperature dependence of the relaxation time τ that is representative of the spin-lattice relaxation (indicated as T_1 in pulsed resonance spectroscopies). In order to investigate the temperature dependence of τ under a static magnetic field where τ is maximized, the studies were also performed at 1.0 T (*vide infra*). The frequency dependence of χ'' are well reproduced with the Debye model (Figures S8-S14) and the extracted values of τ as a function of the temperature for the two selected field values for **1** and **2** are reported in Figure 2a.
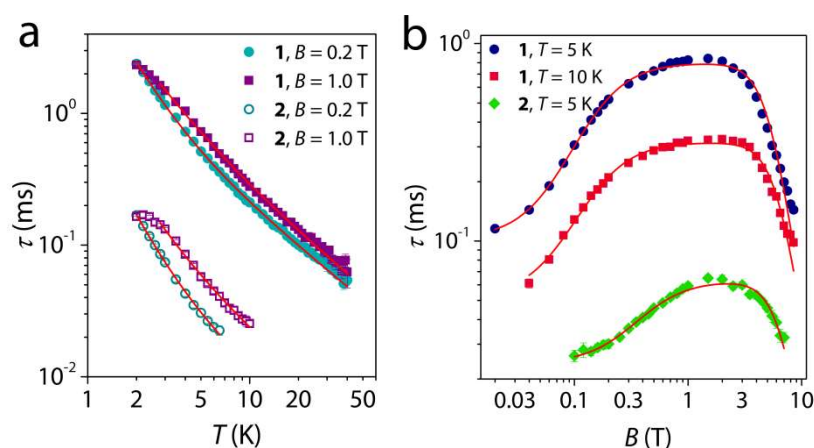

Figure 2. (a) Temperature and (b) field dependence of τ extracted from AC susceptibility measurements for compounds **1** and **2** at different applied static magnetic field values and temperatures (see legends). Solid lines are the best-fits of the models.

1 shows slow magnetic relaxation in the temperature range between 2.0 and 40 K with quite long relaxation times ranging from ca. 2.3 ms at 2.0 K to ca. 0.05 ms at 40 K. **2** exhibits relaxation times in the 0.17–0.025 ms range that are substantially lower with respect to those of **1**. This results in a reduced temperature range where slow magnetic relaxation is detectable (2.0–10 K). Minor differences in the magnitude of τ are observed between 0.2 and 1.0 T, especially for **1**, since τ is almost maximum at 0.2 T (*vide infra* and Figure 2b). The temperature dependence of τ, reported in Figure 2a in a *log(τ) vs log(T)* plot, reveals an increase in the slope at low temperature which is indicative of a phonon-bottleneck effect affecting the direct mechanism of relaxation in concentrated samples.[25] To account for these contributions to the

relaxation, the τ decay was fitted (solid lines in Figure 2a) assuming two sequential steps in the relaxation process: the energy transfer from the spin to the phonon lattice and then its release to the thermostatic bath, accordingly to the Scott and Jefferies model[26]

$$\tau = \frac{1}{aT} + \frac{1}{bT^n} \qquad (1)$$

where a is the coefficient of the direct mechanism, and b and n the coefficient and the exponent of the phonon-bottleneck, respectively. This model satisfactorily reproduces the T dependence of τ with the best-fit parameter reported in Table 1.

Table 1. Best-fit parameters of the model used (eq. 1) to reproduce the temperature dependence of the relaxation time for **1** and **2** at $B = 0.2$ T and 1.0 T.

Compound	B (T)	a (ms^{-1} K^{-1})	b (ms^{-1}K^{-n})	n
1	0.2	0.52(1)	0.11(1)	2.6(1)
	1.0	0.44(2)	0.14(1)	2.1(1)
2	0.2	9.6(6)	1.31(9)	2.7(1)
	1.0	4.9(5)	1.14(3)	2.4(3)

From the values of the extracted coefficients it can be noted that both direct and phonon-bottleneck terms are higher for **2** than for **1**, in agreement with the most effective relaxation observed for **2** (Figure 2a). It should be also noted that the extracted values of the T exponent for the phonon-bottleneck effect, within the 2–3 range, are slightly higher than those usually observed (ca. 2) for classical atom-based inorganic systems.[27]

In order to get better insights on the relaxation mechanisms involved in such compounds, the relaxation time was also investigated as a function of the static magnetic field in a wide field range (0.0–8.5 T) at two different temperatures, 5 and 10 K for **1**, and 5 K for **2** due to instrumental limitations. The relaxation times extracted with the Debye model (Figures S12-S14) for **1** and **2** are reported in Figure 2b. The field dependence of the relaxation time for **1** shows, already at low fields, a rapid increase of τ. It reaches the maximum value at ca. 0.4 T, then it remains almost unchanged up to ca. 3.5 T, and finally starts to decrease at higher fields reaching a minimum at the highest applied field (8.5 T). **2** shows a similar behavior with respect to **1** but with a less abrupt increase of τ as the strength of the field increases, thus resulting in a narrower range where τ is maximized (1.0–3.5 T). This non-monotonous behavior is similar to what already reported for closely related systems,[20,21] and reflects two antagonist effects of the magnetic field. Spin-spin and spin-nuclei interactions promote rapid relaxation at low fields.

These interactions are suppressed by increasing the field due to the lower influence of the hyperfine and spin-spin coupling (*vide infra*). On the other hand, the larger is the energy separation of the two levels the higher is the phonon density with an energy corresponding to this difference, leading to a more efficient spin-phonon direct mechanism of relaxation ($\tau \propto B^4$). To account for these two contributions to the relaxation, the *B* dependence of the relaxation rate (τ^{-1}) for **1** and **2** was reproduced (solid lines in Figure 2b) with the Brons-van Vleck model[28,29]

$$\tau^{-1} = cB^4 + d\frac{1 + eB^2}{1 + fB^2} \qquad (2)$$

This model well reproduces the *B* dependence of τ with the best-fit parameter reported in Table 2.

Table 2. Best-fit parameters of the model used to reproduce the field dependence of the magnetization relaxation rate (equation 2) for **1** at *T* = 5 K and 10 K and **2** at *T* = 5 K.

Compound	*T* (K)	*c* (T^{-4}ms^{-1})	*d* (ms^{-1})	*e* (T^{-2})	*f* (T^{-2})
1	5	$1.8(1) \times 10^{-3}$	10(1)	40(4)	306(60)
	10	$2.1(1) \times 10^{-3}$	19(3)	38(5)	231(60)
2	10	$8.0(6) \times 10^{-3}$	41(1)	5.0(6)	13(2)

The coefficients reported in Table 2 indicates that *i)* the direct mechanism of relaxation (*c* coefficient) is more efficient for **2** with respect to **1**, in accordance with the thermal dependence of τ, *ii)* the ability of the field to suppress the effect of spin-spin and spin-nuclei interactions to the relaxation (*f* coefficient) is lower for **2** than for **1**, in accordance with the less abrupt increase of τ as the field increase and the narrower range where τ is maximized.

CW and Pulsed Electron Paramagnetic Resonance Spectroscopy. While AC susceptometry provides useful information about T_1 as a function of the temperature and the magnetic field in quite concentrated samples (**1** and **2** in this study), pulsed EPR spectroscopy allows to characterize both T_1 and T_m in diluted systems characterized by narrow resonance lines. A common way to achieve this condition is the dispersion of the paramagnetic component in a diamagnetic matrix. With this scope, crystalline dispersions of **1** and **2** in **3** and **4** have been prepared with an amount of paramagnetic component dispersed in the diamagnetic host of ca. 5±1% (**5, 5'** and **6**) (*vide supra*).

The room temperature CW-EPR X-band spectra (9.43 GHz) of compounds **1** and **5**, and **2** and **6** are reported in Figure S15. Compound **1** shows an EPR spectrum where the expected

eight-fold hyperfine splitting of all anisotropic components typical of V^{IV} (^{51}V I = 7/2, abundance 99.76%) is poorly resolved due to line broadening induced by dipolar interactions between the magnetic moments of the paramagnetic V^{IV} ions (Figure S15a). A lower resolution is observed for compound **2**, where only a broad unresolved absorption is observed (Figure S15b). The crystalline dispersions of **1** in **3** (**5**) and **2** in **4** (**6**) dramatically change the EPR spectra. In fact, even if **5** and **6** contain a relatively high concentration of paramagnetic species (ca. 5±1%), they exhibit the expected hyperfine splitting with well-defined narrow lines also at room temperature. Notably, **5** shows very narrow resonance lines that are further narrowed in the deuterated analogue **5'** (Figure S16). Peaks due to the parallel components of the hyperfine coupling are observed at low and high field values, whereas those due to the perpendicular components are observed in the central region.

Spectral simulations[30] were performed at X- and Q-band frequencies on the basis of the following spin Hamiltonian

$$\mathcal{H} = \hat{I} \cdot A \cdot \hat{S} + \mu_B \hat{S} \cdot g \cdot B \qquad (3)$$

The spectrum of **5** can be satisfactorily simulated at both frequencies (Figures 3a and S17a) assuming a collinear rhombic model (*i.e.* x ≠ y ≠ z) with the parameters reported in Table 3. Attempts to simulate the EPR spectra of **6** using a similar rhombic model were unsuccessful. Indeed, although it gave reasonable fits at X-band frequency, notable discrepancies in the positions of the hyperfine transitions and line shapes were observed at Q-band frequency (Figure S18). Therefore, the possibility of a non-collinearity between *A* and *g* tensors, consistent with the triclinic point symmetry of the complex anion,[31] was investigated. A process of trial and error gave spectral simulations in good agreement with the experimental results (Figures 3b and S17b) using the parameters reported in Table 3.

Table 3. Spin-Hamiltonian parameters extracted from simulation of the experimental spectra of **5** and **6**. The Euler angles α, β, γ define the passive rotation of the hyperfine principal axes system into the *g*-matrix principal axes system, $A = R(\alpha, \beta, \gamma) A_{\text{diagonal}} R^+(\alpha, \beta, \gamma)$.

Compound	g_x	g_y	g_z	$|A_x|$ (MHz)	$|A_y|$ (MHz)	$|A_z|$ (MHz)	α, β, γ (°)
5	1.986(1)	1.988(1)	1.970(1)	138(2)	128(2)	413(2)	0, 0, 0
6	1.961(1)	1.971(1)	1.985(1)	299(2)	230(2)	40(5)	−20, −10, 0

* It must be noted that the reference system for the two compounds is different. For **5** the *z* axis can be considered collinear to the V=O bond, while for **6** it is close to the octahedron pseudo-*C₃* symmetry axis, *i.e.* perpendicular to its trigonal faces.

We note that such phenomenon was not previously recognized for tris-dithiolene V^{IV} complexes; the possibility to detect it here is clearly due to the improved resolution of the solid crystalline spectra, together with the multifrequency EPR approach, compared to the frozen solution ones.[19,24] Further confirmation of the goodness of the obtained parameters was provided by the simulation of the room temperature solution spectrum of **6** in the fast motion regime (Figure S19), which allowed to confirm the value of the A_z component, to which the solid state spectra are not very sensitive.

The two compounds are thus characterized by distinctly different spin-Hamiltonian parameters, which reflect the different chemical structure of the V^{IV} ions in **5** and **6**. An empirical correlation between the g_{iso} ($g_{iso} = (g_1+g_2+g_3)/3$) and ^{51}V a_{iso} ($a_{iso} = (A_1+A_2+A_3)/3$) has been proposed to discriminate between $V^{IV}O^{2+}$ and V^{IV} centers.[32] Indeed the spin Hamiltonian parameters of **5** fit well within known values for vanadyl ions, while the values of **6** are representative for V^{IV} centers.

In the EPR spectra of **5** and **5'**, an additional signal exhibiting the typical features of an organic radical ($g = 2.00$) is present. This signal can be ascribed to an impurity of monooxidized uncoordinated dmit$^{\cdot-}$ ligand as tetraphenylphosphonium salt, being it a redox active ligand susceptible of one-electron oxidation.[24] This signal is not observed in **6** most likely as a result of the different synthetic approaches followed for the crystalline dispersion preparation (*vide supra*).

The X- and Q-band echo-detected field-swept (EDFS) EPR spectra for **5** and **6** were recorded at different temperature by using a standard Hahn echo sequence. Figure 3 reports the highest temperature data at the X-band whereas those recorded at the Q-band are reported in Figure S17.
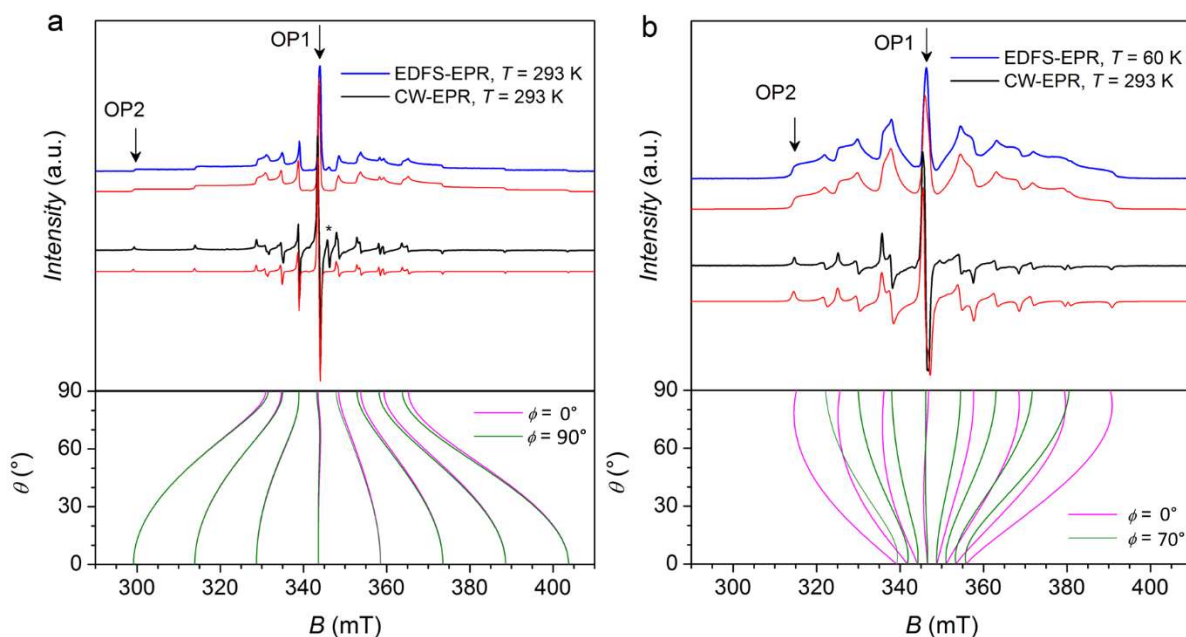
Figure 3. Experimental EDFS- (blue line) and CW- (black line) EPR spectra for **5** (a) and **6** (b) at X-band frequency (9.7 GHz). The spectral simulations corresponding to the spin Hamiltonian parameters reported in Table 3 are shown in red. The arrows indicate the two magnetic field settings at which pulse EPR experiments were performed. The asterisk indicates the signal of an organic radical impurity. The angular dependency profile (θ vs magnetic field) is shown for two angles of ϕ.

As evidenced by the presence of an intense spin-echo, we can anticipate that quantum coherence is expected for **5** up to room temperature. Moreover, the spin Hamiltonian parameters obtained through the simulation of the CW spectrum allow to provide good simulations of the EDFS spectra as well, thus indicating that the entire paramagnetic component of **5** is experiencing the detected coherence. Analogous results are observed for the deuterated analogue **5'**. Interestingly, while **5** shows an intense spin-echo at room temperature, **6** do not show an EDFS spectrum working at the X-band at the same temperature. A spin-echo is only hardly detected working at Q-band (Figure S18). Nonetheless, by lowering the temperature, **6** shows the expected coherence, as could be anticipated on the basis of recent studies performed on **2** in frozen solutions.[19]

Inversion recovery experiments were performed in the 4.5–293 K temperature range for **5**, **5'** and **6** at X and Q-band frequencies to investigate the temperature dependence of the spin-lattice relaxation time T_1. Experiments at X-band were performed at two magnetic field settings: *i)* the so-called powder-like position, $m_I = -1/2$ (OP1), where all molecules are excited due to the negligible angular dependency of the resonance field, and *ii)* the single crystal-like position,

$m_I = -7/2$ (OP2), where only molecules with their z axis within 10° from the field direction are selected (Figure 3). Q-band experiments were instead performed only at the $m_I = -7/2$ position. This because the angular dependency of the EPR spectra for **5** and **6** show that *i)* this position corresponds to a pure transition for both systems allowing for a direct comparison with X-band, and *ii)* a powder-like position is not present at Q-band frequency for both **5** and **6** (Figure S17). The resulting saturation recovery traces were fitted with a stretched monoexponential equation

$$I = I_0 + k_1 exp^{\left[-\left(\frac{\tau_p}{T_1}\right)^{\beta_1}\right]} \qquad (4)$$

and the extracted T_1 values are reported in Figure 4. Only the values obtained at the $m_I = -7/2$ are reported for clarity since no major differences are observed working at the $m_I = -1/2$ observer position (Figure S20).
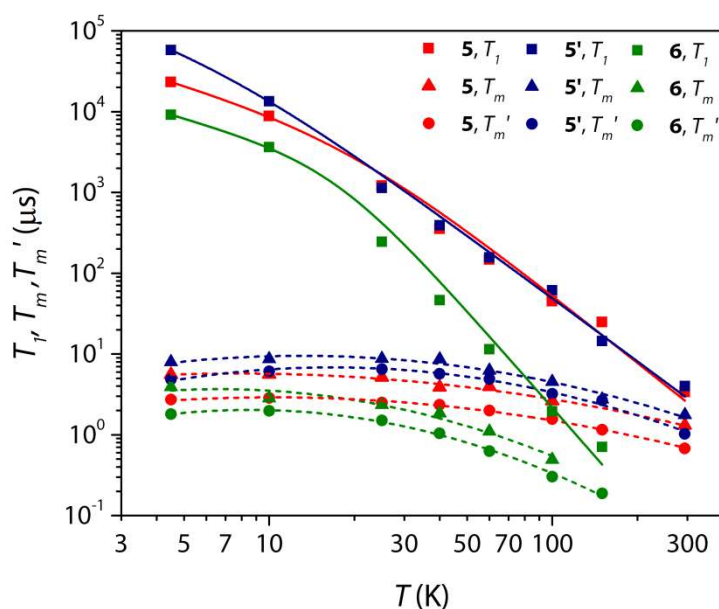

Figure 4. Temperature dependence of T_1, T_m, and T_m' for **5**, **5'** and **6** (see legend) obtained at OP2. Solid lines are the best-fit of the model (see text). Short-dashed lines represent a guide for the eyes. Error bars are within the size of the symbols.

5 and **5'** show similar T_1 values in almost the whole investigated temperature range. Deuteration of the cation increases T_1 only at low temperature (Figure 4), and more significantly at X-band than at Q-band (Tables S2-S7). A moderate increase of T_1 upon deuteration is not unprecedented and can be related either to the different dipolar coupling[33] or to the isotope mass effect.[34] T_1 values for **5** and **5'** are higher than those of **6** in the entire investigated T range, in agreement with what observed with the field dependence of τ from AC susceptibility data on the pure compounds **1** and **2**. This suggests that hyperfine interactions are responsible for the fast relaxation observed in weak or zero applied fields.[35] The thermal variation of T_1 for **5** and

5' shows a slow decrease from the maximum values of ca. 23 ms (**5**) and ca. 58 ms (**5'**) at 4.5 K, to the lowest, but still remarkable values of 3.37 μs (**5**) and 4.03 μs (**5'**) at 293 K. Moving from X- to Q-band (Figure S21) a slight increase of T_1 is observed at the lowest temperatures which is in agreement with the weak field dependence of the relaxation time observed in that range (Figure 2b). The extracted relaxation times from pulsed EPR are, however, almost one order of magnitude longer than those of **1** and **2** from AC susceptibility, as expected for magnetically diluted compounds, and do not show the upturn at low temperature typical of the spin-phonon bottleneck effect observed in concentrated samples. The temperature dependence of T_1 have been modeled assuming two contributions to the relaxation. A direct mechanism dominating at low temperature, as suggested from AC susceptometry, and a Raman-like mechanism dominating at high temperature.

$$T_1^{-1} = aT + bT^n \qquad\qquad (5)$$

The best-fit values for **5** and **5'** give a very low value of the Raman-like exponent $n < 3$, 2.8(4) and 2.6(2). Values of ca. 3 were already observed in closely-related vanadyl-based systems[20,21,36] and are attributed to the involvement of both optical and acoustic phonons to the relaxation.[37] The thermal variation of T_1 for **6** shows a slow decrease from the maximum value of ca. 9 ms up to ca. 15 K, then a more abrupt decrease is observed as the temperature increases, resulting in the lowest detectable value of T_1 of 0.71 μs at 150 K (Figure 4). The temperature dependence of T_1 has been simulated with the same model used for **5** and **5'**. The best-fit values give a Raman-like exponent n of 4.0(5), in agreement with the more abrupt decrease of T_1 that acts as a limiting factor for T_2 (*vide infra*).

To investigate the quantum coherence in details and to quantify the phase memory time, T_m, of **1** and **2** in the doped materials **5** and **5'**, and **6** as a function of the temperature, echo decay experiments were also performed (Figure 5). Remarkably, echo decay traces were detected up to room temperature for **5** and **5'**, with an increased value of T_m for the deuterated analogue (Figure 4). On the contrary, **6** shows echo decay traces up to 150 K with T_m values shorter than those of **5** and **5'** as evidenced by the restricted time scale of the echo decay (Figure 5).
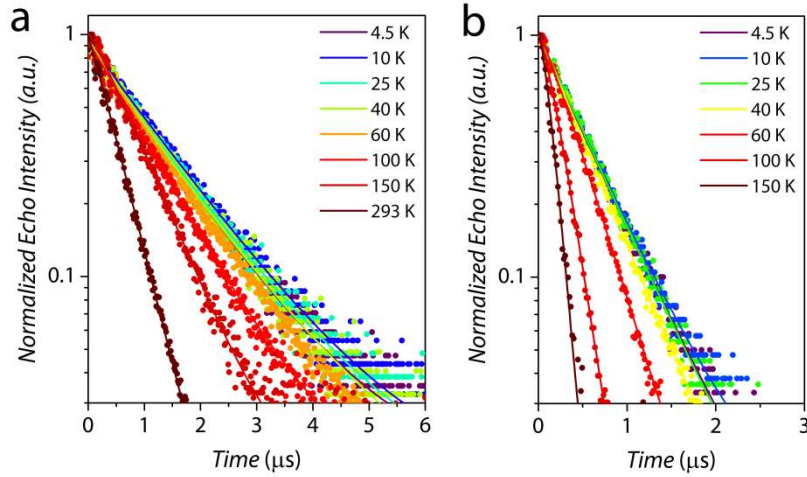
Figure 5. Echo decay traces recorded at the OP1 (X-band) for **5** (a) and **6** (b) at different temperatures (see legend).

The decay traces were fitted using the stretched-exponential equation

$$I = I_0 + k_m exp^{\left[-\left(\frac{2\tau_p}{T_m}\right)^{\beta_m}\right]} \quad (6)$$

as usually done for transition metal systems,[38] where I indicates the echo intensity, $2\tau_p$ is the delay between the initial pulse and the echo detection and β_m is the stretch factor. For sake of comparison transverse relaxation times were also measured by using the Car-Purcell-Meiboom-Gill (CPMG) sequence.[39,40] Phase memory times (T_m') only weakly longer were obtained by CPMG than by two-pulse spin echo (Tables S2). This is in agreement with the expectations, given the relatively high concentration of electron spins in our system[41-43] and the broad EPR spectrum.[44] The temperature dependences of both T_m and T_m' for **5**, **5'** and **6** are reported in Figure 4.

The thermal variation of T_m for **5** and **5'** shows an almost temperature independent behavior in the 4.5–100 K range, with values of T_m and T_m' within the 2.9–1.6 µs and 5.6–2.6 µs ranges for **5**, and within the 6.5–3.2 µs and 8.7–4.5 ranges for **5'**. Then they slowly decrease as the temperature increases reaching remarkable values of 0.68 µs and 1.0 µs (T_m) at room temperature (Figure 4). It should be highlighted that the values of T_m at room temperature for the concentrated dispersion of **5** and **5'** (ca. 5±1%) are slightly higher than values observed to date for transition metal-based molecular qubits in much higher diluted environment, *e.g.* the 0.001% crystalline dispersion of $[P(Ph)_4]_2[Cu(mnt)_2]$ in $[P(Ph)_4]_2[Ni(mnt)_2]$ (0.60 µs)[17] and the 0.1% crystalline dispersion of VOPc in TiOPc (0.83 µs).[21] T_m' values are even higher, being T_m' a better estimation of T_2, but we cannot compare these values with what already reported since most literature reports provide only T_m estimations by Hahn echo experiments.

The thermal variation of T_m and T_m' for **6** shows an almost temperature independent behavior in a limited temperature range (4.3–25 K) with values of T_m and T_m' within the 2.0–1.5 µs and 3.9–2.4 µs ranges, then they slowly decrease as the temperature increases reaching a value of T_m of 0.19 µs at 150 K. The quantum coherence times T_m for **6** are in general lower than those of **5** and **5'**, but the most important result is that they are strongly limited in temperature by the more abrupt decrease of T_1.

To prove that the observed coherence times for **5** and **5'** allow to perform coherent spin manipulations at room temperature, *i.e.* place the spins in any arbitrary superposition of states, nutation experiments were performed at different microwave powers at both X- and Q-bands. Remarkably, Rabi oscillations were clearly observed at room temperature with the expected linear dependence of the Rabi frequency, Ω_R, as a function of the microwave attenuation (Figure 6). Rabi oscillations were instead observed for **6** only at low temperature (Figure S22).
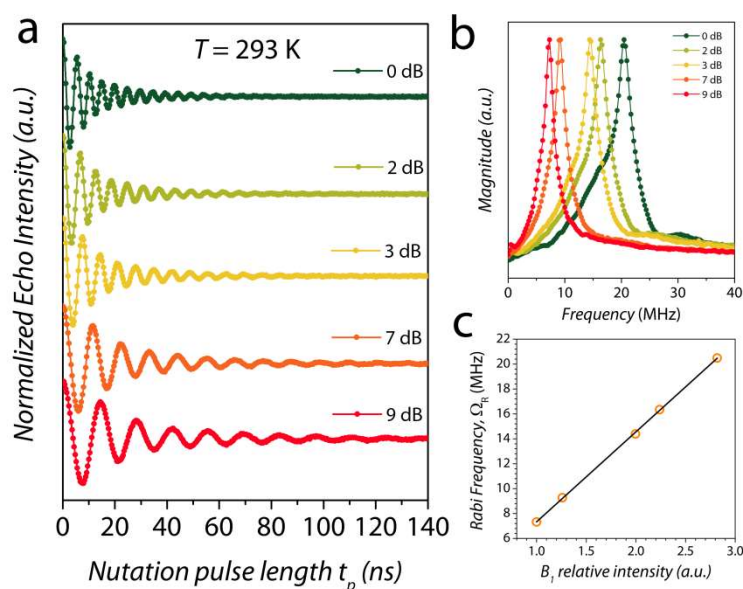

Figure 6. (a) Rabi oscillations recorded for **5** at 293 K for different microwave attenuations (Q-band). (b) Fourier Transform of the Rabi oscillations. (c) Linear dependence of the Rabi frequency (Ω_R) as a function of the relative intensity of the oscillating field B_1.

In order to fully characterize the local environment of the V^{IV} ions in the two compounds, Q-band Mims ENDOR spectra were recorded (Figure S23). The spectra show that in both cases the V^{IV} ions have a similar proton rich environment, with maximum couplings of 3.5(1) MHz for compound **5** and 3.0(1) MHz for compound **6**. Based on a point-dipole approximation and assuming a pure dipolar interaction, these couplings correspond to shortest V⋯H distances of the order of 3.6(1) Å and 3.8(1) Å, respectively. These values are in excellent agreement with the structural findings which reveal shortest V⋯H distances of 3.6(1) Å and

3.8(1) Å for **5** and **6**, respectively. This excludes that the better performances of the vanadyl species are due to a more favorable nuclear spin environment generated by the counterions and highlights the key role of the coordination mode.

This comparative detailed investigation has evidenced significant differences in the dynamic properties of two closely related vanadium(IV) complexes. **2** shows, in general, a faster relaxation with respect to **1**, and this behaviour can be tentatively ascribed to a more pronounced contribution to the SOMO by different orbitals, *i.e.* the ground state is not a pure d_z^2 one. This is demonstrated by the observed non-collinearity of the *A* and *g* tensors as well as by the significant deviation of g_z from the value of 2.00 expected for this geometry. The larger the deviations from the free electron values, the more efficient is the spin-orbit coupling in promoting magnetic relaxation. In this respect, the EPR derived Spin Hamiltonian parameters can also explain the stronger static magnetic field required to slow down the relaxation for **2**. Indeed, the analysis of the eigenvector composition for an applied field of 0.1 T clearly evidences that **2** is characterized by a larger mixing of the states compared to **1**, which is significantly enhanced by the non-collinearity of the *g* and *A* tensors (Figure S24). However, the most relevant difference between the two compounds is the temperature dependence of the spin-lattice relaxation time. Excitation of vibrational modes that can couple to the spin are responsible of the acceleration of the relaxation with increasing temperature. Here, the similar crystallographic cell size and content of the two complexes suggest that acoustic phonons should equally contribute,[45] and cannot be at the origin of this behavior. On the contrary, molecular vibration involving the metal ion coordination sphere are dramatically different due to the presence of the V=O double-bond that resonates at much higher frequencies (ca. 980 cm^{-1}) with respect to the V–S single bonds (in the 400–300 cm^{-1} range). As the largest differences in T_1 are observed at high temperatures, where optical phonons are relevant, spin-vibration coupling seems the dominating effect in determining the remarkable difference in the temperature dependence of T_1.

CONCLUDING REMARKS

The parallel multitechnique investigation of two V^{IV} complexes with nuclear-spin free ligands both in pure phases and diluted in diamagnetic crystalline hosts has revealed significant differences in the spin-lattice relaxation times, which are much longer for the vanadyl complex compared to the tris-chelated one. A poorly efficient mechanism of relaxation seems most often encountered on oxovanadium(IV)-based systems,[20,21,34,46] making this moiety a very useful

building block for the preparation of performing potential molecular qubits. On the contrary, the same metal ion in a different coordination environment, as the distorted octahedral coordination geometry herein investigated, is not capable to retain quantum coherence up to room temperature, as a result of a slightly different Raman-like relaxation mechanism.

Our results represent a first experimental evidence of the proposed importance of the rigidity of the molecular structure in the enhancement of quantum coherence.[17] If the general rule is now rather clear, to develop more performing molecular spin qubits it is crucial to understand in details which vibrational modes are the most effective in promoting spin relaxation. In this regard, state-of-the art *ab initio* calculations combining density functional theory (DFT) and post Hartree-Fock approaches have been recently employed to evaluate the spin-vibration coupling in a square planar copper(II)-based complex in a simplified environment.[47] However, the rationalization of the magnetic relaxation in molecular systems requires an accurate description of the lattice dynamics which is beyond current computation capabilities for those compounds, as the ones herein investigated, which contain bulky counterions. Vanadyl-based neutral complexes of *β*-diketonate ligands, whose phonon spectrum has been recently evaluated and correlated to a giant spin-phonon bottleneck effect at low temperature,[45] appear as more suitable candidates for this scope. A deeper understanding of the relaxation mechanisms taking into account both hyperfine interactions and vibrational modes seems then the winning strategy to enhance quantum coherence in molecular systems.

EXPERIMENTAL SECTION

General remarks. 4,5-bis(benzoylthio)-1,3-dithiole-2-thione,[48] d_{20}-tetraphenylphosphonium bromide,[17] and pyridinium molybdenyl(V) pentachloride,[49] were synthesized accordingly to the literature procedures. Tetraphenylphoshonium bis(1,3-dithiole-2-thione-4,5-dithiolate)zincate(II) was obtained accordingly to the literature procedure[48] by replacing tetraethylammonium bromide with tetraphenylphosphonium bromide. All others reagents were purchased and used as received.

Synthesis.

[(Ph)₄P]₂[VO(dmit)₂] (1). An aqueous solution (5 mL) of $VOSO_4 \cdot xH_2O$ (0.245 g, 1.5 mmol) was added dropwise to a methanol solution (35 mL) of sodium 1,3-dithiole-2-thione-4,5-dithiolate (Na₂dmit) obtained *in situ* by reacting 4,5-bis(benzoylthio)-1,3-dithiole-2-thione (1.22 g, 3.0 mmol) and sodium (0.150 g, 6.5 mmol). A methanol solution (5 mL) of

tetraphenylphoshonium bromide (1.70 g, 4.0 mmol) was added dropwise to the resulting solution with precipitation of **1** as a red-brown microcrystalline solid. The precipitate was separated from the mother liquor by vacuum filtration, washed several times with methanol, and then with diethyl ether. Yield 74%. Compound **1** was crystallized in acetone to give red-orange shiny crystals suitable for X-ray analysis. Elemental anal. calcd for $C_{54}H_{40}OP_2S_{10}V$: C, 56.97; H, 3.54; found: C, 56.75; H, 3.38. FT-IR ($\bar{\upsilon}_{max}/cm^{-1}$, KBr pellet): 3166 vw, 3087vw, 3074vw, 3053w, 3035vw, 3016vw, 3004vw, 2987vw, 1583w, 1570vw, 1558vw, 1541vw, 1481w, 1440s, 1434s, 1338w, 1315w, 1186w, 1163w, 1107s, 1043m, 1023s, 995m, 956m (ν V=O), 902w, 892w, 854vw, 852vw, 758m, 752m, 723s, 689s, 526vs, 464m.

[(Ph)₄P]₂[V(dmit)₃] (2). VCl₃ (0.069 g, 0.44 mmol) was added in portion to a stirred methanol solution (50 mL) of [(Ph)₄P]₂[Zn(dmit)₂] (0.500 g, 0.44 mmol). After few minutes a brown microcrystalline solid of **2** starts to precipitate. The mixture was stirred for 1 hour at room temperature, then the precipitate was separated from the mother liquor by vacuum filtration, washed several times with methanol, and then with diethyl ether. Yield 60%. Compound **2** was crystallized by diffusion of diethyl ether in acetone to give black shiny crystals suitable for X-ray analysis. Elemental anal. calcd for $C_{57}H_{40}P_2S_{10}V$: C, 51.91; H, 3.06; found: C, 52.07; H, 2.57. FT-IR ($\bar{\upsilon}_{max}/cm^{-1}$, KBr pellet): 3163 vw, 3076vw, 3053w, 3016vw, 3006vw, 2987vw, 1583w, 1570vw, 1558vw, 1541vw, 1481w, 1435s, 1396w, 1338w, 1315w, 1186w, 1163w, 1109s, 1049vs, 1028s, 995m, 891w, 845vw, 752m, 723s, 689s, 615w, 526s, 469m, 445w.

[(Ph)₄P]₂[MoO(dmit)₂] (3). A methanol solution (10 mL) of HPy₂MoOCl₅ (1.125 g, 2.5 mmol) was added dropwise to a methanol solution (50 mL) of sodium 1,3-dithiole-2-thione-4,5-dithiolate (Na₂dmit) obtained *in situ* by reacting 4,5-bis(benzoylthio)-1,3-dithiole-2-thione (2.04 g, 5.0 mmol) and sodium (0.280 g, 12.0 mmol). A methanol solution (10 mL) of tetraphenylphoshonium bromide (2.50 g, 6.0 mmol) was added dropwise to the resulting solution with precipitation of **3** as a brown microcrystalline solid. The precipitate was separated from the mother liquor by vacuum filtration and washed several times with methanol, and then with diethyl ether. Yield 63%. Compound **3** was crystallized in acetone to give orange-brown shiny crystals suitable for X-ray analysis. Elemental anal. calcd for $C_{54}H_{40}OP_2S_{10}Mo$: C, 54.80; H, 3.41; found: C, 53.96; H, 3.14. FT-IR ($\bar{\upsilon}_{max}/cm^{-1}$, KBr pellet): 3166 vw, 3087vw, 3074vw, 3053w, 3035vw, 3016vw, 3004vw, 2987vw, 1583w, 1570vw, 1558vw, 1541vw, 1481w, 1448m, 1440m, 1435s, 1338w, 1315w, 1186w, 1163w, 1107s, 1043m, 1024m, 995m, 922m (ν Mo=O), 889w, 883w, 854vw, 852vw, 758m, 752m, 723s, 689s, 526vs, 464m.

[(Ph)₄P]₂[Ti(dmit)₃] (4). An aqueous solution (10 mL) of $TiCl_4$ (0.302 g, 1.6 mmol) was added dropwise to a methanol solution (50 mL) of sodium 1,3-dithiole-2-thione-4,5-dithiolate (Na_2dmit) obtained *in situ* by reacting 4,5-bis(benzoylthio)-1,3-dithiole-2-thione (2.04 g, 5.0 mmol) and sodium (0.280 g, 12.0 mmol). A methanol solution (10 mL) of tetraphenylphoshonium bromide (1.70 g, 4.0 mmol) was added dropwise to the resulting solution with precipitation of **4** as a black-purple microcrystalline solid. The precipitate was separated from the mother liquor by vacuum filtration, washed few times with methanol, and then with diethyl ether. Yield 42%. Elemental anal. calcd for $C_{57}H_{40}OP_2S_{15}Ti$: C, 52.03; H, 3.06; found: C, 51.78; H, 2.94. FT-IR ($\bar{v}_{max}/cm^{-1}$, KBr pellet): 3163 vw, 3076vw, 3053w, 3016vw, 3006vw, 2987vw, 1583w, 1570vw, 1558vw, 1541vw, 1481w, 1435s, 1396w, 1338w, 1315w, 1186w, 1163w, 1107s, 1049vs, 1028s, 995m, 904w, 891w, 845vw, 752m, 723s, 689s, 615w, 526s, 467m, 445w.

[(Ph)₄P]₂[VO₀.₀₅MoO₀.₉₅(dmit)₂] (5). A methanol solution (10 mL) of $VOSO_4 \cdot xH_2O$ (0.041 g, 0.25 mmol) and HPy_2MoOCl_5 (0.450 g, 2.25 mmol) was added dropwise to a methanol solution (50 mL) of sodium 1,3-dithiole-2-thione-4,5-dithiolate (Na_2dmit) obtained *in situ* by reacting 4,5-bis(benzoylthio)-1,3-dithiole-2-thione (2.04 g, 5.0 mmol) and sodium (0.280 g, 12.0 mmol). A methanol solution (10 mL) of tetraphenylphoshonium bromide (2.50 g, 6.0 mmol) was added dropwise to the resulting solution with precipitation of **5** as a brown microcrystalline solid. The precipitate was separated from the mother liquor by vacuum filtration, washed few times with methanol, and then with diethyl ether. Yield 52%. Elemental anal. calcd for $C_{57}H_{40}OP_2S_{15}Ti$: C, 52.03; H, 3.06; found: C, 51.78; H, 2.94. FT-IR ($\bar{v}_{max}/cm^{-1}$, KBr pellet): 3166 vw, 3087vw, 3074vw, 3053w, 3035vw, 3016vw, 3004vw, 2987vw, 1583w, 1570vw, 1558vw, 1541vw, 1481w, 1448m, 1440m, 1435s, 1338w, 1315w, 1186w, 1163w, 1107s, 1043m, 1024m, 995m, 956m (ν V=O), 922m (ν Mo=O), 889w, 883w, 854vw, 852vw, 758m, 752m, 723s, 689s, 526vs, 464m. X-ray fluorescence (XRF) analysis was used to estimate the effective percentage of doping by comparing the intensity of the XRF intensity of vanadium K_α emission of compound **5** to a calibration curve obtained by mixing weighted amounts of the pure compounds (**1** and **3**) in the 1-20% concentration range. This was found to be 5(1)% of VO^{2+} and 95(1)% of MoO^{2+}.

[d₂₀-(Ph)₄P]₂[VO₀.₀₅MoO₀.₉₅(dmit)₂] (5'). Compound **5'** was obtained by following the same procedure reported for **5** by using perdeutereted tetraphenylphoshonium bromide instead of tetraphenylphoshonium bromide. Yield 49%. FT-IR ($\bar{v}_{max}/cm^{-1}$, KBr pellet): 2289 vw, 2282vw, 2265vw, 2255vw, 1545w, 1533vw, 1448m, 1308m, 1061m, 1043s, 1024m, 962vw, 954w (ν

V=O), 927m (v Mo=O), 889vw, 883vw, 872vw, 837m, 829w, 694w, 548w, 542w, 500vs, 463w, 445vw. X-ray fluorescence (XRF) analysis was used to estimate the effective percentage of doping by comparing the intensity of the XRF intensity of vanadium $K\alpha$ emission of compound **5'** to a calibration curve obtained by mixing weighted amounts of the pure compounds (**1** and **3**) in the 1-20% concentration range. This was found to be 5(1)% of VO^{2+} and 95(1)% of MoO^{2+}.

[(Ph)₄P]₂[V₀.₀₅Ti₀.₉₅(dmit)₂] (6). 2 (0.075 g, 0.0057 mmol) and **4** (0.1425 g, 0.108 mmol) were dissolved in 120 mL of acetone. The solution was filtrated to remove few undissolved particles and the solvent evaporated under reduced pressure. **6** precipitates as a black-purple microcrystalline solid. Yield: quantitative. Elemental anal. calcd for $C_{57}H_{40}OP_2S_{15}Ti_{0.95}V_{0.05}$: C, 52.02; H, 3.06; found: C, 52.10; H, 2.91. FT-IR ($\bar{v}_{max}$/cm^{-1}, KBr pellet): 3163 vw, 3076vw, 3053w, 3016vw, 3006vw, 2987vw, 1583w, 1570vw, 1558vw, 1541vw, 1481w, 1435s, 1396w, 1338w, 1315w, 1186w, 1163w, 1107s, 1049vs, 1028s, 995m, 904w, 891w, 845vw, 752m, 723s, 689s, 615w, 526s, 467m, 445w. X-ray fluorescence (XRF) analysis was used to estimate the effective percentage of doping by comparing the intensity of the XRF intensity of vanadium $K\beta$ emission of **6** to a calibration curve obtained by mixing weighted amounts of the pure compounds (**2** and **4**) in the 1-10% concentration range. This was found to be 6(1)% of V^{IV} and 94(1)% of Ti^{IV}.

Characterization. C, H, N analyses were performed with a *CHN-S Flash E1112 Thermofinnigan* analyzer. FT-IR spectra were performed on KBr pellets and collected with a *Shimadzu-8400S* spectrophotometer. X-ray fluorescence analyses were performed with a *WD-XRF Rigaku PrimusII* spectrophotometer.

Single Crystal X-Ray Crystallography. Single crystal X-ray diffraction measurements were performed on an *Oxford Xcalibur PX Ultra - Onyx CCD* diffractometer, using an Enhance Ultra X-ray graphite-monochromated CuKα radiation (λ = 1.540 Å). The structures were solved by direct methods (SHELXS-97) and refined on F^2 with full-matrix least squares (SHELXL-97),[50] using the Wingx software package.[51] All non-H atoms were refined with anisotropic displacement parameters. Graphical material was prepared using Mercury CSD 3.5.[52] A summary of the crystallographic data and the structure refinement for compounds **1**–**3** is reported in Table 4.

Table 4. Summary of X-ray crystallographic data for **1**, **2**, and **3**.

	1	2	3
Empirical formula	$C_{54}H_{40}OP_2S_{10}V$	$C_{57}H_{40}P_2S_{15}V$	$C_{54}H_{40}OP_2S_{10}Mo$
Formula weight	1138.34	1318.67	1183.34
Crystal size, mm	$0.60 \times 0.40 \times 0.40$	$0.50 \times 0.40 \times 0.10$	$0.20 \times 0.20 \times 0.10$
Crystal system	Monoclinic	Monoclinic	Monoclinic
Space group	*C2/c*	*P2₁/c*	*C2/c*
a, Å	20.4747(5)	24.5669(3)	19.9651(3)
b, Å	12.7283(4)	13.8150(1)	12.5335(1)
c, Å	20.6032(5)	18.1309(2)	20.8994(2)
α, deg.	90	90	90
β, deg.	95.297(2)	111.014(1)	94.260(1)
γ, deg.	90	90	90
V, Å^3	5346.4(2)	5744.2(1)	5215.3(1)
Z	4	4	4
T, K	293(2)	100(2)	100(2)
ρ (calc), Mg/m^3	1.414	1.525	1.507
μ, mm^{-1}	6.071	7.379	6.691
θ range, deg.	4.31–61.86	4.14–72.42	4.24–70.56
GooF	1.024	1.050	1.106
$R1$	0.0587	0.0372	0.0280
$wR2$	0.0678	0.0910	0.0624

$R1 = \Sigma||F_O|-|F_C||/\Sigma|F_O|$, $wR2 = [\Sigma[w(F_O{}^2-F_C{}^2)^2]/\Sigma[w(F_O{}^2)^2]]^{1/2}$, $w = 1/[\sigma^2(F_O{}^2) + (aP)^2 + bP]$, where $P = [\max(F_O{}^2,0) + 2F_C{}^2]/3$.

Full crystallographic data for the solved structures have been deposited in the Cambridge Crystallographic Data Centre with CCDC numbers 1482025 (**1**), 1482026 (**2**), 1482027 (**3**), 1482028 (**7**), respectively.

Powder X-Ray Crystallography. Wide-Angle Powder X-Ray Diffraction (PXRD) patterns on polycrystalline samples were recorded on a *Bruker New D8 Advance DAVINCI* diffractometer in a theta-theta configuration equipped with a linear detector. The scans were collected within the range 5–40° (*2θ*) using CuK_α radiation (λ = 1.540 Å). Simulated patterns were generated from the atomic coordinates of the single-crystal structure solutions using the Mercury CSD 3.5 software[52] (copyright CCDC, http://www.ccdc.cam.ac.uk/mercury/) using a FWHM (full width at half maximum) of 0.10 and a *2θ* step of 0.025.

Electron Paramagnetic Resonance. CW X-Band EPR spectra of all samples were recorded on a *Bruker Elexsys E500* spectrometer equipped with a SHQ cavity (ν = 9.43 GHz). Low temperature measurements were obtained using an *Oxford Instruments ESR900* continuous

flow helium cryostat. Pulsed EPR measurements were carried out with a *Bruker Elexsys E580* at X-band ($v \cong 9.70$ GHz) equipped with a flexline dielectric ring ENDOR resonator (*Bruker EN 4118X-MD4*). Temperatures between 4.5 and 250 K were obtained with *an Oxford Instruments CF935* continuous flow helium cryostat. Echo detected field swept EPR spectra were recorded by using the Hahn Echo pulse sequence ($\pi/2—\tau—\pi—\tau—echo$) with fixed interpulse delay time $\tau = 200$ ns, $t_{\pi/2} = 16$ ns and $t_\pi = 32$ ns. Phase memory times were measured both by the Hahn Echo sequence upon increasing the interpulse delay τ starting from $\tau = 98$ ns, and by a CPMG sequence with a fixed interpulse delay 2τ in the echo train and $\tau = 800$ ns. Typical pulse lengths were $t_{\pi/2} = 40$ ns and $t_\pi = 80$ ns. Spin-lattice relaxation times were measured using the standard inversion recovery sequence ($\pi—t_d—\pi/2—\tau—\pi—\tau—echo$), with $\pi/2 = 16$ ns. The uncertainty in T_1 estimated from replicate measurements was 5%–10% depending upon the signal-to-noise ratio at a given temperature-field combination. Nutation measurements were performed with a nutation pulse (t_p) of variable length followed by a Hahn echo sequence (t_p-$t_d—\pi/2—\tau—\pi—\tau—echo$) with $t_d \gg T_m$ (*i.e.* $t_d = 7$ μs for 4 K and 2 μs for room temperature measurements). The interpulse delay τ was 200 ns and the pulse length of the detection sequence was adjusted depending on the attenuation level of B_1.

Magnetic measurements. AC (alternate current) susceptibility measurements were performed in the temperature range 2.0–40 K with applied magnetic fields up to 8.5 T on polycrystalline samples of compounds **1** (55.71 mg) and **2** (53.10 mg), by using a *Quantum Design Physical Property Measurement System (PPMS)* equipped with a AC susceptometer operating in the 10 Hz–10 kHz frequency range. Susceptibility data were corrected for the sample holder previously measured using the same conditions and for the diamagnetic contributions as deduced by using Pascal's constant tables.[53]

ASSOCIATED CONTENT

Supporting Information
The Supporting Information is available free of charge on the ACS Publications website at DOI: XXXXX. Additional Figures and Tables as mentioned in the text.

AUTHOR INFORMATION

Corresponding Authors
*E-mail: roberta.sessoli@unifi.it

*E-mail: matteo.atzori@unifi.it

Notes

The authors declare no competing financial interest.

REFERENCES

1. Troiani F.; Affronte, M. *Chem. Soc. Rev.* **2011**, *40*, 3119–3129.

2. Aromì, G.; Aguila, D.; Gamez, P.; Luis F.; Roubeau, O. *Chem. Soc. Rev.* **2012**, *41*, 537–546.

3. Nielsen M. A.; Chuang I. L. *Quantum Computation and Quantum Information*; Cambridge University Press: Cambridge, 2000.

4. Ladd, T. D.; Jelezko, F.; Laflamme, R.; Nakamura, Y.; Monroe C.; O'Brien J. L. *Nature* **2010**, *464*, 45–53.

5. Kennedy, T. A.; Colton, J. S.; Butler, J. E.; Linares R. C.; Doering, P. J. *Appl. Phys. Lett.* **2003**, *83*, 4190–4192.

6. Balasubramanian, G.; Neumann, P.; Twitchen, D.; Markham, M.; Kolesov, R.; Mizuochi, N.; Isoya, J.; Achard, J.; Beck, J.; Tissler, J.; Jacques, V.; Hemmer, P. R.; Jelezko F.; Wrachtrup, J. *Nat. Mater.* **2009**, *8*, 383–387.

7. Pla, J. J.; Tan, K. Y.; Dehollain, J. P.; Lim, W. H.; Morton, J. J. L.; Jamieson, D. N.; Dzurak, A. S.; Morello, A. *Nature* **2012**, *489*, 541–545.

8. Tyryshkin, A. M.; Tojo, S.; Morton, J. J. L.; Riemann, H.; Abrosimov, N. V.; Becker, P.; Pohl, H.-J.; Schenkel, T.; Thewalt, M. L. W.; Itoh, K. M.; Lyon, S. A. *Nat. Mater.* **2012**, *11*, 143–147.

9. Gatteschi, D.; Sessoli R.; Villain J. *Molecular nanomagnets*; Oxford University Press: Oxford, UK, 2006.

10. Fataftah, M. S.; Zadrozny, J. M.; Coste, S. C.; Graham, M. J.; Rogers, D. M.; Freedman, D. E. *J. Am. Chem. Soc.* **2016**, *138*, 1344–1348.

11. Pedersen, K. S.; Ariciu, A.-M.; McAdams, S.; Weihe, H.; Bendix, J.; Tuna F.; Piligkos, S. *J. Am. Chem. Soc.* **2016**, *138*, 5801–5804.

12.   Shiddiq, M.; Komijani, D.; Duan, Y.; Gaita-Ariño, A.; Coronado, E.; Hill, S. *Nature* **2016**, *531*, 348–351.

13.   DiVincenzo, D. P. *Fortschritte der Physik*, **2000**, *48*, 771–783.

14.   Takahashi, S.; Tupitsyn, I. S.; van Tol, J.; Beedle, C. C.; Hendrickson, D. N.; Stamp, P. C. E. *Nature*, **2011**, *476*, 76–79.

15.   Ferrando-Soria, J.; Moreno Pineda, E.; Chiesa, A.; Fernandez, A.; Magee, S. A.; Carretta, S.; Santini, P.; Vitorica-Yrezabal, I. J.; Tuna, F.; Timco, G. A.; McInnes, E. J. L.; Winpenny, R. E. P. *Nat. Commun.*, **2016**, *7,* 11377.

16.   Warner, M.; Din, S.; Tupitsyn, I. S.; Morley, G. W.; Stoneham, A. M.; Gardener, J. A.; Wu, Z.; Fisher, A. J.; Heutz, S.; Kay, C. W. M.; Aeppli, G. *Nature* **2013**, *503*, 504–508.

17.   Bader, K.; Dengler, D.; Lenz, S.; Endeward, B.; Jiang, S.-D.; Neugebauer, P.; van Slageren, J. *Nat. Commun.*, **2014**, *5,* 15841.

18.   Zadrozny, J. M.; Niklas, J.; Poluektov, O. G.; Freedman, D. E. *J. Am. Chem. Soc.* **2014**, *136*, 15841–15844.

19.   Zadrozny, J. M.; Niklas, J.; Poluektov, O. G.; Freedman, D. E. *ACS Cent. Sci.* **2015**, *1*, 488.

20.   Tesi, L.; Lucaccini, E.; Cimatti, I.; Perfetti, M.; Mannini, M.; Atzori, M.; Morra, E.; Chiesa, M.; Caneschi, A.; Sorace, L.; Sessoli, R. *Chem. Sci.* **2015**, *7*, 2074–2083.

21.   Atzori, M.; Tesi, L.; Morra, E.; Chiesa, M.; Sorace, L.; Sessoli, R. *J. Am. Chem. Soc.* **2016**, *138*, 2154–2157.

22.   Matsubayashi, G.-E.; Nojo, T.; Tanaka, T. *Inorg. Chim. Acta* **1988**, *154*, 133–135.

23.   Matsubayashi, G.; Akiba, K.; Tanaka, T. *Inorg. Chem.*, **1988**, *27*, 4744–4749.

24.   Sproules, S.; Weyhermüller, T.; DeBeer, S.; Wieghardt, K. *Inorg. Chem.* **2010**, *49*, 5241–5261.

25.   Van Vleck, J. H. *Physical Review* **1941**, *59*, 724–729.

26.   Scott, P. L.; Jeffries, C. D. *Physical Review*, **1962**, *127*, 32–51.

27.   Standeley, K. J.; Vaughan, R. A. *Plenum Press, New York*, **1969**, 199–236.

28.   Van Vleck, J. H. *Physical Review*, **1940**, *57*, 426–447.

29.   De Vroomen, A. C.; Lijphart, E. E.; Prins, D. Y. H.; Marks, J.; Poulis, N. J. *Physica*, **1972**, *61*, 241–249.

30.   Stoll, S.; Schweiger, A. *J. Magn. Reson.* **2006**, *178*, 42–55.

31.   Pilbrow, J. R.; Lowrey, M. R. *Reports on Progress in Physics*, **1980**, *43*, 433.

32.   Jakes, P.; Eichel, R.-A. *Molecular Physics*, **2012**, *110*, 277–282.

33. Sato, H; Bottle, S. E.; Blinco, J. P.; Micallef, A. S.; Eaton, G. R.; Eaton, S. S. *J. Magn. Reson.* **2008**, *191*, 66–77.

34. Owenius, R.; Terry, G. E.; Williams, M. J.; Eaton, S. S.; Eaton, G. R. *J. Phys. Chem. B*, **2004**, *108*, 9475–9481.

35. Gómez-Coca, S.; Urtizberea, A.; Cremades, E.; Alonso, P. J.; Camón, A.; Ruiz, E. ; Luis, F. *Nat. Commun.* **2014**, *5*, 4300.

36. Du, J.-L.; Eaton, G. R.; Eaton, S. S. *J. Magn. Reson. A*, **1996**, *119*, 240–246.

37. Shrivastava, K. N. *Phys. Status Solidi B* **1983**, *117*, 437–458.

38. Eaton, S. S.; Eaton, G. R. In *Distance Measurements in Biological Systems by EPR*; Berliner, L. J., Eaton, G. R. and Eaton, S. S., Eds.; Springer US: Boston, MA, **2002**, 29–154.

39. Carr, H. Y.; Purcell, E. M. *Physical Review* **1954**, *94*, 630–638.

40. Meiboom, S.; Gill, D. *Review of Scientific Instruments*, **1958**, *29*, 688–691.

41. Harbridge, J. R.; Eaton, S. S.; Eaton, G. R. *J. Magn. Reson.* **2003**, *164*, 44–53.

42. de Lange, G. ; Wang, Z. H.; Ristè, D.; Dobrovitski, V. V. ; Hanson, R. *Science* **2010**, *330*, 60–63.

43. Zaripov, R.; Vavilova, E.; Miluykov, V.; Bezkishko, I.; Sinyashin, O.; Salikhov, K.; Kataev, V.; Büchner, B. *Physical Review B* **2013**, *88*, 094418.

44. Kurshev, V. V.; Raitsimring, A. M. *J. Magn. Reson.* **1990**, *88*, 126–129.

45. Tesi, L.; Lunghi, A.; Atzori, M.; Lucaccini, E.; Sorace, L.; Totti, F.; Sessoli, R. *Dalton Trans.* **2016**, final acceptance step.

46. Bader, K.; Winkler, M.; van Slageren, J. *Chem. Commun.* **2016**, *52*, 3623–3626.

47. Escalera-Moreno, L.; Suaud, N.; Gaita-Ariño, A. arXiv:1512.05690.

48. Hansen, T. K.; Becher, J.; Jørgensen, T.; Varma, K. S.; Khedekar, R.; Cava, M. P. *Organic Syntheses*, **1996**, *73*, 270.

49. Hanson, G. R.; Brunette, A. A.; McDonell, A. C.; Murray, K. S.; Wedd, A. G. *J. Am. Chem. Soc.* **1981**, *103*, 1953–1959.

50. Sheldrick, G. M. *Programs for the Refinement of Crystal Structures, University of Göttingen, Göttingen, Germany*, **1996**.

51. Farrugia, L. *J. Appl. Crystallogr.* **1999**, *32*, 837–838.

52. Macrae, C. F.; Bruno, I. J.; Chisholm, J. A.; Edgington, P. R.; McCabe, P.; Pidcock, E.; Rodriguez-Monge, L.; Taylor, R.; van de Streek, J.; Wood, P. A. *J. Appl. Crystallogr.* **2008**, *41*, 466–470.

53.   Bain, G. A.; Berry, J. F. *J. Chem. Educ.* **2008**, *85*, 532.

TABLE OF CONTENTS GRAPHIC

Oxovanadium(IV)   *VS*   Vanadium(IV)